Title

Lesion detection and quantification performance of the Tachyon-I time-of-flight PET scanner: phantom and human studies

Journal

Physics in Medicine and Biology, 63(6)

ISSN

0031-9155

Authors

Zhang, Xuezhu
Peng, Qiyu
Zhou, Jian
et al.

Publication Date

2018-03-01

DOI

10.1088/1361-6560/aab0f3

Peer reviewed

HHS Public Access

Author manuscript

Phys Med Biol. Author manuscript; available in PMC 2019 March 16.

Published in final edited form as:

Phys Med Biol. ; 63(6): 065010. doi:10.1088/1361-6560/aab0f3.

Lesion Detection and Quantification Performance of the Tachyon-I Time-of-Flight PET Scanner: Phantom and Human Studies

Xuezhu Zhang[1], **Qiyu Peng**[1,2], **Jian Zhou**[1], **Jennifer S. Huber**[2], **William W. Moses**[2], and **Jinyi Qi**[1]

[1]Department of Biomedical Engineering, University of California, Davis, California 95616, United States

[2]Lawrence Berkeley National Lab, Berkeley, California 94720, United States

Abstract

The first generation Tachyon PET (Tachyon-I) is a demonstration single-ring PET scanner that reaches a coincidence timing resolution of 314 ps using LSO scintillator crystals coupled to conventional photomultiplier tubes (PMT). The objective of this study was to quantify the improvement in both lesion detection and quantification performance resulting from the improved time-of-flight (TOF) capability of the Tachyon-I scanner. We developed a quantitative TOF image reconstruction method for the Tachyon-I and evaluated its TOF gain for lesion detection and quantification. Scans of either a standard NEMA torso phantom or healthy volunteers were used as the normal background data. Separately scanned point source and sphere data were superimposed onto the phantom or human data after accounting for the object attenuation. We used the bootstrap method to generate multiple independent noisy datasets with and without a lesion present. The signal-to-noise ratio (SNR) of a channelized Hotelling observer (CHO) was calculated for each lesion size and location combination to evaluate the lesion detection performance. The bias versus standard deviation trade-off of each lesion uptake was also calculated to evaluate the quantification performance. The resulting CHO-SNR measurements showed improved performance in lesion detection with better timing resolution. The detection performance was also dependent on the lesion size and location, in addition to the background object size and shape. The results of bias versus noise trade-off showed that the noise (standard deviation) reduction ratio was about 1.1–1.3 over the TOF 500 ps and 1.5–1.9 over the non-TOF modes, similar to the SNR gains for lesion detection. In conclusion, this Tachyon-I PET study demonstrated the benefit of improved time-of-flight capability on lesion detection and ROI quantification for both phantom and human subjects.

1. Introduction

Time-of-Flight (TOF) Positron Emission Tomography (PET) can enhance the diagnostic accuracy of reconstructed images by improving the signal-to-noise ratio (SNR) of PET data (Moses 2003, Conti 2011, Conti and Eriksson 2013, Eriksson and Conti 2015). The TOF information can be incorporated into the reconstruction process to localize each annihilation

Correspondence to: Jinyi Qi.

event within a certain range (e.g. 9 cm FWHM for TOF 600 ps scanner) along a line-of-response (LOR), which can effectively reduce the amplification of statistical noise. This increased statistical efficiency can improve the image quality with the same number of detected events, or it can be used to reduce the injected dose or scan time to alleviate the patient discomfort and imaging cost. A better timing resolution can also have an even greater benefit for a long axial FOV scanner due to its increasing path length of more oblique lines of response inside a subject (Zhang *et al* 2017). The work of TOF PET can be traced back to the early 1980s (Budinger 1983), but it regained attention in the late 1990s after the development of fast scintillators with high photon detection efficiency (Moses and Ullisch 2006, Moses *et al* 2010). Currently all major PET manufacturers offer TOF capability as a standard imaging configuration.

Many studies have been conducted to assess the benefit of TOF PET over non-TOF PET (Surti *et al* 2007, Jakoby *et al* 2011, Schaefferkoetter *et al* 2013). The TOF gain on variance reduction or signal-to-noise ratio can be calculated using an analytic formula with a simplified model based on a uniform cylinder (Tomitani 1981, Snyder *et al* 1981). A simple noise reduction factor can be estimated using the approximate expression $\sqrt{D/\Delta x}$ (Budinger 1983), where D is the size or diameter of the emission distribution and Δx is the spatial localization uncertainty (FWHM) with $\Delta x = c\Delta t/2$ due to the limited coincidence timing resolution Δt to detect two coincident photons at the speed of light c. Recent works have shown TOF provides better image quality and fast convergence of image reconstruction, and the TOF benefit is higher in larger or heavier objects (Surti *et al* 2006, Karp *et al* 2008, Surti and Karp 2009, Surti *et al* 2011, Kadrmas *et al* 2009, El Fakhri *et al* 2011). Most existing studies were conducted using commercial systems with a TOF resolution of 450–600 ps and focused on lesion detection. One paper by Daube-Witherspoon *et al.* examined lesion quantification using their LaBr3 system with a TOF resolution of 375 ps (Daube-Witherspoon *et al* 2014). In this paper, we examine the benefits of TOF for a TOF resolution as low as 314 ps.

In order to evaluate the benefit of improved timing resolution for lesion detection and quantification using real data, we have built a demonstration TOF PET called the Tachyon-I (Peng *et al* 2015). It is a single-ring scanner formed by 192 detector modules with a ring diameter of 78 cm. Each detector module consists of a 2×1 array of 6.15×6.15×25.4 mm^3 Lutetium Oxyorthosilicate (LSO) crystals coupled to a Hamamatsu R-9800 photomultiplier tube (PMT). The axial length of this scanner is 6 mm. The Tachyon-I achieves a coincidence timing resolution of 314±20 ps, which is significantly better than the resolution of 450–600 ps provided by the current commercial clinical TOF PET scanners with a PMT coupled L(Y)SO design. The superior timing capability results in a localization uncertainty of ~4.7 cm, which provides significantly improved noise/variance reduction. The energy resolution is 19.6% and the lead shields are equipped to restrict the scatter and random events coming from the outside of FOV. Details of the system configuration and characterization have been reported previously (Peng *et al* 2015). A second-generation system using digital photomultiplier detectors is under development to further improve the timing performance (Peng and Moses 2016).

In this work, we focused on quantifying the benefit of the improved TOF performance achieved by the Tachyon-I scanner. Both detection and quantitative tasks were studied. Numerical observers were employed to calculate the signal-to-noise ratio for lesion detection. The quantitative task was evaluated by calculating the bias of the uptake in a lesion region of interest (ROI) versus variance trade-off from one hundred independent realizations of reconstructed images.

2. Materials and methods

2.1. Image reconstruction and system modeling

We developed quantitative image reconstruction software for the Tachyon-I scanner. A statistically based iterative TOF list-mode image reconstruction method was used to take advantage of the accurate statistical and physical models of the PET imaging process (Qi and Leahy 2006, Zhou and Qi 2011). To assess the accuracy of our system resolution recovery model used for this scanner, we scanned a ^{22}Na source (1.0 mm diameter and 0.5-mm long cylinder, 50 μCi) at various radial distances from the center of the FOV and reconstructed the point source data to estimate the point spread function (PSF). Figure 1 shows the reconstructed images of the point source data. We can see that the PSF is nearly independent of the radial offset, indicating that the system matrix accurately models the detector blurring effect in the whole FOV.

2.2. Normalization and attenuation correction

We used a component-based normalization that includes crystal efficiencies and geometric response (Badawi and Marsden 1999). The normalization factors were estimated from a blank scan using an external ^{22}Na point source (1.0 mm diameter and 1-mm long cylinder, 250 μCi) rotated concentrically near the inner surface of the scanner (Figure 2(a)). To obtain the attenuation correction factors, we performed a transmission scan using the same orbiting source. The transmission data were separated from emission data using a radially dependent TOF window (Yamamoto *et al* 1983, Mollet *et al* 2012) and sinogram mask appropriate for the point source position (rod windowing) (Huesman *et al* 1988). Figure 2(b) shows the timing bin histogram of post-injection-transmission-scan events in all LORs passing through the radial center, demonstrating that emission events (gray color) can be well separated from transmission events (blue). Figure 2(c) shows a sample sinogram mask with LORs passing through the point source at a specific spatial location and the corresponding sinogram measured at the same time, thus demonstrating that most events are from the point source and fall inside the rod window. By using the TOF information and counting only the events in the rod window, the crosstalk between the emission and transmission data can be effectively eliminated. Figure 2(d) shows the reconstructed transmission image of a NEMA IEC Body phantom (Data Spectrum Corporation, Hillsborough, NC, USA) at 511 keV. The estimated attenuation coefficient ($0.009\pm0.0012\ mm^{-1}$) is very close to that of water.

2.3. Scatters and randoms corrections

In the experiments, we used a coincidence timing window (CTW) of 4.5 ns to cover a 67.5 cm transaxial FOV. We implemented a TOF single-scatter simulation algorithm (SSS) to estimate the scatters mean (Watson 2007). For random correction, we estimated the randoms

mean using a wide (90 ns) delayed window and scaled the resulting delayed random events by 0.024/90 for each TOF bin (24 ps) and 4.5/90 for non-TOF bin. This scaling resulted in a variance reduction factor of 3,750 for TOF and 20 for nonTOF, which is more than sufficient for randoms correction based on an analysis given in (Qi and Huesman 2002). Figure 3 shows the radial profiles of the measured TOF sinograms of the NEMA IEC Body Phantom and the estimated mean of the scattered and random events, both summed over all projection angles (see Section 3.1 for more details on the phantom experiment). The good match between the tails of the measured sinogram and the estimated mean of scatters and randoms indicates that our estimation of scatters and randoms were relatively accurate for this scanner. Quantitative comparison showed that the root mean squared error in the tail region between the measured and estimated sinograms was 16.3%, relative to the total number of measured events in the tail region. The estimated scatter fraction and random fraction were 15.4% and 9.2%, respectively, for the NEMA body phantom (with 14.28 mCi initial activity).

3. Evaluation Studies

We used both phantom and human subject data to quantitatively evaluate the benefit of the improved TOF resolution achieved by the Tachyon-I scanner.

3.1. Phantom Study

To generate the lesion present (H1) and lesion absent (H0) datasets, we scanned a NEMA IEC Body Phantom filled with 14.28 mCi ^{18}F solution for 8-hours. A total of 13 million events were detected. To generate multiple realizations of the uniform background, we randomly sampled a mean of 1 million events from the 13 million total detected events and repeated the procedure 100 times (Haynor and Woods 1989, Dahlbom 2002). To simulate cancerous lesions, we individually scanned three spherical hot inserts with diameters of 2-mm, 10-mm or 17-mm at different radial offsets (0, 60 and 120 mm) — acquiring about the same number events for each spherical insert and location (>1Mevents per location). By separately scanning the phantom background and hot spheres, we could attenuate the lesion data by the attenuation map of the body and adjust the contrast of the lesion to a suitable level for the detection task, which has been shown to mimic real patient data (Daube-Witherspoon *et al* 2014, El Fakhri *et al* 2007). Similarly, the measured sphere data were randomly sampled to generate 100 independent realizations of each lesion size and location combination. This resampling method is similar to that used in the work by Daube-Witherspoon et al (Daube-Witherspoon *et al* 2014). The number of events from each hot lesion was adjusted so that the contrast of the lesions to background was 8 for the 2-mm insert and 3 for the 10-mm and 17-mm inserts. The ratio between the total number of measured events and sampled events was between 250 and 1,874 for all inserts.

3.2. Human Subjects data

Because the phantom study cannot accurately provide the non-homogeneous tracer uptake and anatomical tissue variations in human populations, we also acquired human subject data. We recruited four healthy volunteers (2 normal weight (70 – 80 kg) and 2 heavy weight (85 – 100 kg)) and conducted ^{18}F-FDG PET imaging studies using the Tachyon-I scanner. All

the human subject studies were performed under a protocol approved by the institution review board. Each study consisted of two sequential 10-minute transmission and 30-minute emission scans over the chest and abdominal regions after a 5 mCi radiotracer injection and one-hour uptake time. We chose two artificial lesion locations “A” and “B” in the chest region and abdominal region. The previously scanned datasets of the point source (1.0-mm ^{22}Na) and two spherical inserts (10-mm and 17-mm in diameter) were combined with the human subjects data to obtain the lesion present (H1) datasets, similar to our phantom study. Due to the relatively low counts of the human subjects data (0.1–0.6 million events per scan), we used a bootstrap method to generate 100 independent realizations of background data by resampling the measured events with replacement. We also generated 100 independent realizations of the lesion data for each lesion size and location combination. The number of events from each hot lesion was adjusted so to have comparable SNR (i.e., smaller lesion with higher contrast and larger lesion with lower contrast).

3.3. Performance comparison

We compared the performance of the Tachyon-I scanner with the performance of 500-ps TOF PET and non-TOF PET scanners. To simulate a TOF PET scanner with a 500-ps timing resolution, we blurred the time difference of each list-mode event by adding a zero-mean Gaussian random variable with a standard deviation of 165 ps ($\frac{\sqrt{500^2 - 314^2}}{2\sqrt{2\ln 2}}$). Two tasks were used for the comparison: (1) a lesion detection study using a numerical observer and (2) a lesion quantification study using the bias and noise trade-off. All data were reconstructed using the ML-EM algorithm (no subsets) (Shepp and Vardi 1982, Lange and Carson 1984) with all correction factors included in the forward model. The image array consisted of 255 × 255, 3.0 mm square pixels. Since the lesion detectability also depended on the spatial resolution of reconstruction algorithm, we evaluated the performance over a range of iterations.

3.4. Lesion detection analysis

In this study, we used a channelized Hotelling observer (CHO) to measure the lesion detectability in a signal-known-exactly, background-known-exactly (SKE-BKE) task. CHO has been shown to have good correlation with human visual performances (Barrett and Myers 2003). The test statistic and signal-to-noise ratio (SNR) of CHO were respectively computed by

$$\eta\mathrm{CHO}(\hat{x}) = z' U' \sum^{-1} (U\hat{x} + n) \quad (1)$$

$$\mathrm{SNR}^2[\eta\mathrm{CHO}(\hat{x})] = z' U' \sum^{-1} Uz \quad (2)$$

where $\hat{x}$ is a reconstructed image; z represents the expected reconstructed profile of the lesion presence H_1 and lesion absence H_0 ($z = E[\hat{x}|H_1] - E[\hat{x}|H_0]$); U denotes a set of frequency-selective channels mimicking the human visual system; Σ is the covariance of the

channel outputs; and n is the internal channel noise which models the uncertainty in the human detection process with mean zero (Yang *et al* 2014). Three square channel functions were used here (Barrett and Myers 2003). Since the convergence rate of the ML-EM algorithm depends on the TOF resolution, the iteration number of the ML-EM algorithm was chosen to maximize the CHO-SNR for each lesion and TOF resolution individually.

3.5. Lesion quantification analysis

In region of interest (ROI) quantification, we drew lesion ROIs based on the reconstructed images of the sphere-only data and then applied ROI to the reconstructed images with background. We calculated the bias, which is defined as the difference between the reconstructed/observed mean ROI activity $\hat{x}_{roi}$ and the true activity $\hat{x}_{true}$:

$$\text{Bias}\,\% = \frac{\bar{x}_{roi} - \bar{x}_{true}}{\bar{x}_{true}} \quad (3)$$

The noise was calculated as the normalized standard deviation of N realizations of ROI values (N=100):

$$\text{STD}\,\% = \frac{\sqrt{\frac{1}{N-1}\sum_{i=1}^{N}(\bar{x}_i - \bar{x}_{roi})}}{\bar{x}_{true}} \quad (4)$$

At a given bias level (accuracy), STD measures the reproducibility (precision) of the ROI quantification. A lower STD would result in less intra-group variation and provide higher statistical power in differentiating normal and abnormal ROI uptakes. Therefore, we use the STD ratio at a fixed bias level to measure the TOF benefit. Specifically, we first plotted the bias versus STD curve for each inserted lesion. We then computed the STD ratio at a fixed bias level between different TOF resolutions. After calculating the STD ratio over a range of bias levels, we plotted the STD ratio as a function of bias. For human subject studies, because we did not know the ground truth of the human background value, we quantified the bias for the added hot lesion by measuring the difference between the lesion-present reconstruction and the lesion-absent reconstruction and comparing the result with the known sphere uptake.

4. Results

4.1. Phantom Study

4.1.1. Lesion detection performance—Figure 4(a) shows the reconstructed images of one realization of the 2-mm lesion combined with the NEMA phantom. The green arrows point to the locations of the lesion. In the 314-ps images (top row in each panel), the lesion had the highest activity and the noise was low. In comparison, there were many noisy pixels with higher intensity than the lesion in the 500-ps and non-TOF images (middle row and bottom row in each panel, respectively). Figure 4 also shows the reconstructed images of one realization of the 10-mm (b) and 17-mm (c) hot spheres in the NEMA phantom using 314-

ps, 500-ps and non-TOF data. All hot lesions were easily identifiable and more pronounced in the TOF images, but they were not so in the non-TOF reconstructions. Figure 5 shows the bar plots of the maximum CHO-SNR values and Table 1 shows the corresponding TOF gain between the different cases. For each case, we computed the SNR of CHO for the lesion detection at all iterations. The maximum SNR values shown in Figure 5 were used for calculating the TOF benefit. For the 2-mm lesion at the FOV center, the 314-ps TOF outperformed the 500-ps TOF with a SNR gain of 1.3. When the lesion was close to the edge of phantom, the gain reduced to 1.1. The SNR gains over the non-TOF case were 1.7 and 1.5 at the center and edge of the phantom, respectively. For the 10-mm lesion, the SNR gain between 314-ps and 500-ps was 1.1, which is less than the gain for the 2-mm lesion — indicating the dependence of the TOF benefit on lesion size. In general, the SNR gain was higher for a smaller lesion, but a larger lesion had a higher SNR.

4.1.2. ROI quantification performance—Figure 6 shows the bias versus standard deviation (STD) trade-off curves for the ROIs of different sizes and locations. It demonstrates that the 314-ps TOF provided lower absolute bias at fixed STD for all ROIs. For a given bias value, Figure 7 shows that the STD reduction ratio between 314 and 500 ps was 1.4 for the 2-mm lesion at the central region and reduced to 1.2 when the lesion was close to the edge of the phantom. We also examined the bias versus STD trade-off for the larger 10-mm and 17-mm lesions. The results showed similar STD reduction factors between 314-ps TOF and 500-ps TOF as those for the 2-mm lesion.

4.2. Human Subjects Study

Figures 8 (a) and (b) show reconstructed images of the chest scans and abdominal scans with hot lesions (point source, 10-mm and 17-mm spheres) at two locations (A and B). While each dataset only contained a few hundred thousand events due to the low sensitivity of the single-ring scanner, we can clearly see the myocardium region in the TOF reconstruction images, demonstrating good image quality. By visual comparison, the inserted lesions are easier to identify in the TOF reconstructions than in the non-TOF reconstructions, indicating better timing resolution improves the lesion visibility.

4.2.1. Lesion detection performance—Figure 9 shows the maximum CHO-SNR across different iterations for all cases (three lesion sizes, two locations, four subjects). Although some differences in the SNR value existed between the four subjects, better TOF resolution generally resulted in higher SNR. The ratios between the maximum SNR of different TOF resolutions are listed in Table 2. The SNR gain of 314 ps over 500 ps timing resolution was about 1.1–1.2 across all lesion sizes and subjects, similar to our phantom study. The SNR gain over the non-TOF mode was between 1.5 and 1.9. We also observed that the reconstruction algorithm converged faster with better timing resolution, since it takes fewer iterations to reach the peak SNR.

4.2.2. ROI quantification performance—Figure 10 shows the averaged STD ratio versus bias for quantifying the uptake in the 10-mm and 17-mm spheres (averaged over two locations and four subjects). It shows that better timing resolution reduced the standard

deviation in ROI quantification. For a given bias value, the STD reduction factor offered by 314-ps TOF was 1.2 over 500-ps TOF, and 1.8–1.9 over the non-TOF mode.

5. Discussion

In this study, we evaluated the performance gain provided by the Tachyon-I scanner with a timing resolution of 314 ps. The task-based studies using real data from the NEMA phantom and human subjects demonstrated the benefit of improved TOF on both lesion detection and ROI quantification. The experiments showed that the better TOF capability could improve image quality with higher SNR for lesion detection and lower noise for quantification.

The Tachyon-I's TOF resolution of 314 ps corresponds to a 4.71-cm localization uncertainty along each LOR. Theoretical prediction using the simple formula $\sqrt{D/\Delta x}$ indicates a noise reduction factor $\sqrt{(22+29)/2/4.7} = 2.3$ over the non-TOF mode for the NEMA phantom, where D is the the average length of the short axis (22 cm) and long axis (29 cm) of the phantom. A more conservative formula — that takes into account of the Gaussian timing profile — predicts a gain of 1.9 over the non-TOF mode (Tomitani 1981, Eriksson and Conti 2015). Our measured TOF gain of 1.5–1.9 over nonTOF from both phantom and human studies was close to the conservative prediction. The slight difference could be due to the iterative reconstruction algorithm and/or the variation in the background activity. The theoretical prediction also shows a TOF gain $\sqrt{500/314} = 1.26$ between 314-ps TOF and 500-ps TOF. This prediction was also confirmed by our study, which measured a TOF gain between 1.1 and 1.3. Furthermore, our experimental results showed that the TOF gain depended on lesion size and location, in addition to the background activity distribution.

In comparison to previous studies that evaluated TOF benefits using commercial whole-body PET scanners with a TOF resolution ranging from 550 ps to 675 ps (Karp *et al* 2008, Kadrmas *et al* 2009, Surti and Karp 2009, El Fakhri *et al* 2011, Schaefferkoetter *et al* 2013), our study is the first to evaluate TOF benefit down to 314 ps TOF resolution using real physical phantom and human data. Our experimental results also complement previous simulation studies, e.g., (Surti *et al* 2006, Eriksson and Conti 2015, Cao et al 2010), which examined the TOF benefit down to 200 ps TOF resolution using uniform cylindrical phantoms.

There are some limitations in this study. The main limitation is that the sensitivity of the Tachyon-I scanner is very low because it is a single-ring scanner. As a result, the number of counts obtained from the human subjects scans were much less than that obtained by a clinical PET scanner with 15–20 cm axial FOV. To generate multiple realizations, we needed to use the bootstrap method by resampling the list-mode data with replacement. While useful for estimating the variance, the resulting data could not reduce the bias in the original measurements. In comparison, the phantom data were generated by sampling 1 million events out of 13 million detected events, which provided better accuracy in the estimation. A detailed comparison of bootstrap methods can be found in (Lartizien *et al* 2010).

6. Conclusion

The purpose of building the Tachyon-I scanner was to demonstrate and quantify the benefit of improved time-of-flight capability. We acquired phantom and human subjects scans using the Tachyon-I scanner and evaluated performance gains in both lesion detection and ROI quantification tasks. Our results showed that the Tachyon-I PET scanner with 314-ps timing resolution substantially outperformed existing PET scanners with a 1.1–1.3 fold SNR gain and noise reduction over 500-ps TOF and a 1.5–1.9 fold gain over non-TOF scanners for both physical phantom and human subject data. The TOF gain varied with background activity distribution, lesion size and location, and was also task dependent.

Acknowledgments

This work was supported in part by the Director, Office of Science, Office of Biological and Environmental Research, Biological Systems Science Division, U.S. Department of Energy under contract DE-AC02-05CH11231, in part by the National Institutes of Health, National Institute of Biomedical Imaging and Bioengineering, under Grant R01EB006085 and R01EB000194.

References

Badawi RD, Marsden PK. Developments in component-based normalization for 3D PET. Phys. Med. Biol. 1999; 44:571–594. [PubMed: 10070802]

Barrett, HH., Myers, KJ. Foundations of Image Science. New York: Wiley and Sons; 2003.

Budinger TF. Time-of-flight positron emission tomography: status relative to conventional PET. J. Nucl. Med. 1983; 24:73–6. [PubMed: 6336778]

Cao N, Huesman RH, Moses WW, Qi J. Detection performance analysis for time-of-flight PET. Phys. Med. Biol. 2010; 55:6931–6950. DOI: 10.1088/0031-9155/55/22/021 [PubMed: 21048292]

Conti M. Focus on time-of-flight PET: the benefits of improved time resolution. Eur. J. Nucl. Med. Mol. Imaging. 2011; 38:1147–1157. DOI: 10.1007/s00259-010-1711-y [PubMed: 21229244]

Conti M, Eriksson L. Estimating Image Quality for Future Generations of TOF PET Scanners. IEEE Trans. Nucl. Sci. 2013; 60:87–94. DOI: 10.1109/TNS.2012.2233214

Dahlbom M. Estimation of image noise in PET using the bootstrap method. IEEE Trans. Nucl. Sci. 2002; 49:2062–2066.

Daube-Witherspoon ME, Surti S, Perkins AE, Karp JS. Determination of Accuracy and Precision of Lesion Uptake Measurements in Human Subjects with Time-of-Flight PET. J. Nucl. Med. 2014; 55:602–607. [PubMed: 24604909]

El Fakhri G, Santos PA, Badawi RD, Holdsworth CH, Van Den Abbeele AD, Kijewski MF. Impact of Acquisition Geometry, Image Processing, and Patient Size on Lesion Detection in Whole-Body 18F-FDG PET. J. Nucl. Med. 2007; 48:1951–1960. DOI: 10.2967/jnumed.108.007369 [PubMed: 18006613]

El Fakhri G, Surti S, Trott CM, Scheuermann J, Karp JS. Improvement in lesion detection with whole-body oncologic time-of-flight PET. J. Nucl. Med. 2011; 52:347–353. DOI: 10.2967/jnumed.110.080382 [PubMed: 21321265]

Eriksson L, Conti M. Randoms and TOF Gain revisited. Phys. Med. Biol. 2015; 60:1613–1623. [PubMed: 25615713]

Gong K, Majewski S, Kinahan PE, Harrison RL, Elston Brian F, Manjeshwar R, Dolinsky S, Stolin AV, Brefczynski-Lewis JA, Qi J. Designing a compact high performance brain PET scanner-simulation study. Phys Med Biol. 2016; 61:3681–97. doi: DOI: 10.1088/0031-9155/61/10/3681 [PubMed: 27081753]

Haynor DR, Woods SD. Resampling estimates of precision in emission tomography. IEEE Trans. Med. Imaging. 1989; 8:337–343. [PubMed: 18230533]

Huesman RH, Derenzo SE, Cahoon JL, Geyer AB, Moses WW, Uber DC, Vuletich T, Budinger TF. Orbiting transmission source for positron tomography. IEEE Trans. Nucl. Sci. 1988; 35:735–739. DOI: 10.1109/23.12822

Jakoby BW, Bercier Y, Conti M, Casey ME, Bendriem B, Townsend DW. Physical and clinical performance of the mCT time-of-flight PET/CT scanner. Phys Med Biol. 2011; 56:2375–89. DOI: 10.1088/0031-9155/56/8/004 [PubMed: 21427485]

Kadrmas DJ, Casey ME, Conti M, Jakoby BW, Lois C, Townsend DW. Impact of time-of-flight on PET tumor detection. J. Nucl. Med. 2009; 50:1315–23. DOI: 10.2967/jnumed.109.063016 [PubMed: 19617317]

Karp J, Surti S, Daube-Witherspoon M, Muehllehner G. Benefit of time-of-flight in PET: experimental and clinical results. J. Nucl. Med. 2008; 49:462–70. DOI: 10.1109/4233.681168 [PubMed: 18287269]

Lange, Carson. EM reconstruction algorithms for emission and transmission tomography. J Comput. Assist. Tomogr. 1984; 8:306–16. [PubMed: 6608535]

Lartizien C, Aubin JB, Buvat I. Comparison of Bootstrap Resampling Methods for 3-D PET Imaging. IEEE Transactions on Medical Imaging. 2010; 29(7):1442–1454. [PubMed: 20409989]

Mollet P, Keereman V, Clementel E, Vandenberghe S. Simultaneous MR-Compatible Emission and Transmission Imaging for PET Using Time-of-Flight Information. IEEE Trans. Med. Imaging. 2012; 31:1734–42. [PubMed: 22948340]

Moses WW. Time of flight in PET revisited. IEEE Trans. Nucl. Sci. 2003; 50:1325–1330. DOI: 10.1109/TNS.2003.817319

Moses WW, Ullisch M. Factors Influencing Timing Resolution in a Commercial LSO PET Camera. IEEE Trans. Nucl. Sci. 2006; 53:78–85. DOI: 10.1109/TNS.2005.862980

Moses WW, Janecek M, Spurrier MA, Szupryczynski P, Choong W-S, Melcher CL, Andreaco M. Optimization of a LSO-based detector module for time-of-flight PET. IEEE Trans. Nucl. Sci. 2010; 57:1570–6. [PubMed: 21738262]

Peng Q, Choong W-S, Vu C, Huber JS, Janecek M, Wilson D, Huesman RH, Qi J, Zhou J, Moses WW. Performance of the Tachyon Time-of-Flight PET Camera. IEEE Trans. Nucl. Sci. 2015; 62:111–119. DOI: 10.1109/TNS.2014.2375176 [PubMed: 26594057]

Peng, Q., Moses, WW. Development of Tachyon Time-of-Flight PET Cameras; IEEE Nuclear Science Symposuim and Medical Imaging Conference; 2016. p. M16E-14

Qi J, Leahy RM. A theoretical study of the contrast recovery and variance of MAP reconstructions from PET data. IEEE Trans. Med. Imag. 1999; 18:293–305.

Qi J, Leahy RM. Resolution and noise properties of MAP reconstruction for fully 3D PET. IEEE Trans. Med. Imaging. 2000; 19:493–506. [PubMed: 11021692]

Qi J, Huesman RH. Theoretical study of lesion detectability of MAP reconstruction using computer observers. IEEE Trans. Med. Imag. 2001; 20:815–822.

Qi J, Huesman RH. Scatter Correction for Positron Emission Mammography. Phys. Med. Biol. 2002; 47:2759–2772. [PubMed: 12200937]

Qi J. Analysis of lesion detectability in Bayesian emission reconstruction with nonstationary object variability. IEEE Trans. Med. Imaging. 2004; 23:321–9. [PubMed: 15027525]

Qi J, Huesman RH. Theoretical Study of Penalized-Likelihood Image Reconstruction for Region of Interest Quantification. IEEE Trans. Med. Imaging. 2006; 25:640–8. [PubMed: 16689267]

Qi J, Huesman RH. Penalized maximum-likelihood image reconstruction for lesion detection. Phys Med Biol. 2006; 51:4017–29. [PubMed: 16885621]

Qi J, Leahy RM. Topical Review: Iterative reconstruction techniques in emission computed tomography. Phys. Med. Biol. 2006; 51(15):R541–78. DOI: 10.1088/0031-9155/51/15/R01 [PubMed: 16861768]

Schaefferkoetter J, Casey M, Townsend D, El Fakhri G. Clinical impact of time-of-flight and point response modeling in PET reconstructions: a lesion detection study. Phys. Med. Biol. 2013; 58:1465–78. DOI: 10.1088/0031-9155/58/5/1465 [PubMed: 23403399]

Shepp L, Vardi Y. Maximum likelihood reconstruction for emission tomography. IEEE Trans. Med. Imag. 1982; 1:113–22. DOI: 10.1109/TMI.1982.4307558

Snyder DL, Thomas LJ, Ter-Pogossian MM. A mathematical model for positron-emission tomography systems having time-of-flight measurements. IEEE Trans. Nucl. Sci. 1981; NS-28:3575–3583.

Siddon RL. Fast calculation of the exact radiological path for a three-dimensional CT array. Med. Phys. 1985; 12:252–5. [PubMed: 4000088]

Surti S, Karp JS, Popescu LM, Daube-Witherspoon ME, Werner M. Investigation of time-of-flight benefit for fully 3-D PET. IEEE Trans. Med. Imag. 2006; 25:529–538.

Surti S, Kuhn A, Werner M, Perkins A, Kolthammer J, Karp J. Performance of Philips Germini TF PET/CT scanner with special consideration for its time-of-flight imaging capabilities. J. Nucl. Med. 2007; 48:471–80. [PubMed: 17332626]

Surti S, Karp JS. Experimental evaluation of a simple lesion detection task with time-of-flight PET. Phys. Med. Biol. 2009; 54:373–84. [PubMed: 19098351]

Surti S, Scheuermann J, El Fakhri G, Daube-Witherspoon ME, Lim R, Abi-Hatem N, Moussallem E, Benard F, Mankoff D, Karp JS. Impact of time-of-flight PET on whole-body oncologic studies: a human observer lesion detection and localization study. J Nucl Med. 2011; 52:712–9. DOI: 10.2967/jnumed.110.086678 [PubMed: 21498523]

Tomitani T. Image reconstruction and noise evaluation in photon time-of-flight assisted positron emission tomography. IEEE Trans. Nucl. Sci. 1981; 28:4852–9.

Vunckx K, Zhou L, Matej S, Defrise M, Nuyts J. Fisher information-based evaluation of image quality for time-of-flight PET. IEEE Trans. Med. Imaging. 2010; 29:311–21. [PubMed: 19709969]

Watson CC. Extension of Single Scatter Simulation to Scatter Correction of Time-of-Flight PET. IEEE Trans. Nucl. Sci. 2007; 54:1679–1686. DOI: 10.1109/TNS.2007.901227

Yamamoto M, Ficke DC, Ter-Pogossian MM. Effect of the Software Coincidence Timing Window in Time-of-Flight Assisted Positron Emission Tomography. IEEE Trans. Nucl. Sci. 1983; 30:711–714. DOI: 10.1109/TNS.1983.4332362

Yang L, Zhou J, Ferrero A, Badawi RD, Qi J. Regularization design in penalized maximum-likelihood image reconstruction for lesion detection in 3D PET. Phys Med Biol. 2014; 59:403–19. DOI: 10.1088/0031-9155/59/2/403 [PubMed: 24351981]

Zhang X, Zhou J, Cherry SR, Badawi RD, Qi J. Quantitative image reconstruction for total-body PET imaging using the 2-meter long EXPLORER scanner. Phys. Med. Biol. 2017; 62:2465–2485. [PubMed: 28240215]

Zhou J, Qi J. Fast and efficient fully 3D PET image reconstruction using sparse system matrix factorization with GPU acceleration. Phys. Med. Biol. 2011; 56:6739–57. [PubMed: 21970864]

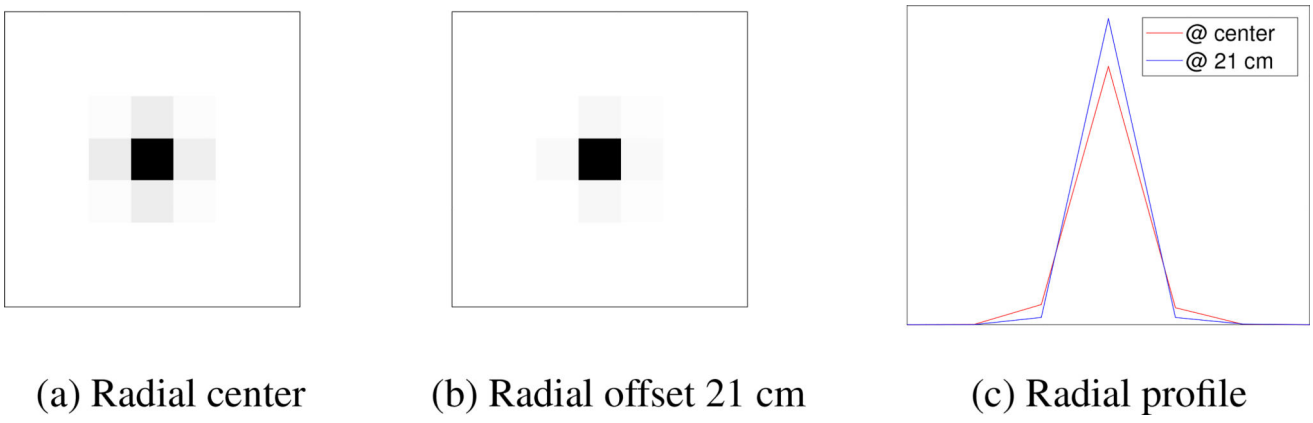

Figure 1.

Reconstructed point-source images at (a) radial center and (b) 21 cm radial offset, and (c) the radial profiles through the point-source images. The voxel size is 3.0 mm.

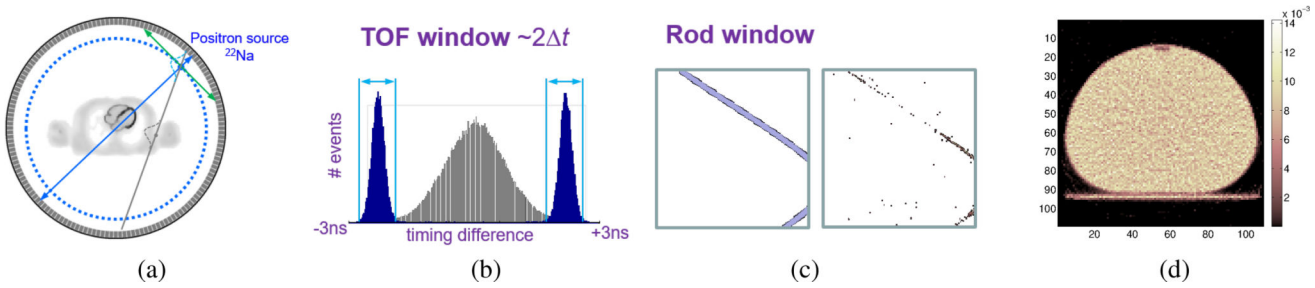

Figure 2.

(a) External orbiting source used to obtain the normalization and attenuation correction factors. (b) Timing bin histogram of events from a post-injection transmission scan along all central LORs (blue color: transmission events; gray color: emission events). (c) An example of the rod window (left image) and the measured sinogram at the same time (right image). (d) Reconstructed attenuation coefficient image of a NEMA torso phantom.

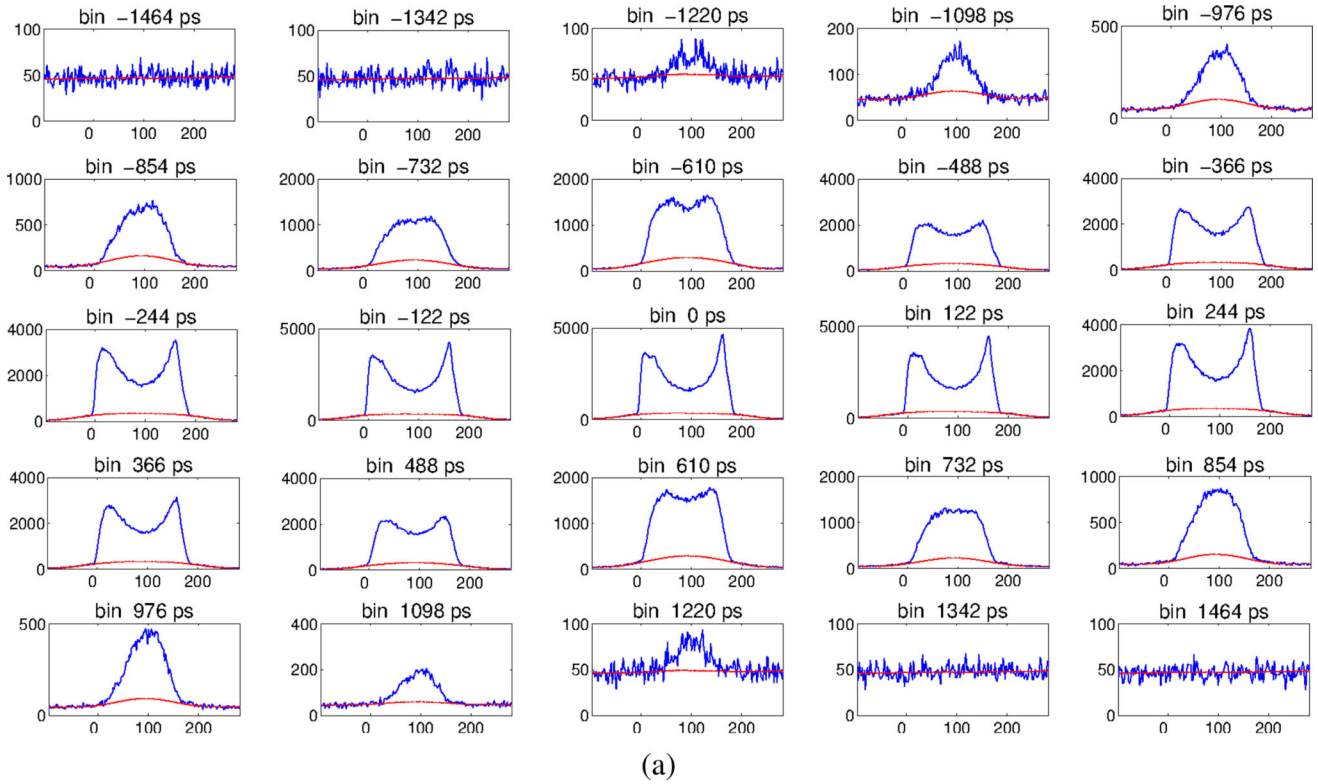

Figure 3.

Radial profiles of the TOF sinogram summed over all projection angles. Each TOF bin shown here is 122-ps wide. Blue curves denote measured data and red curves denote the estimated mean of scattered and random events.

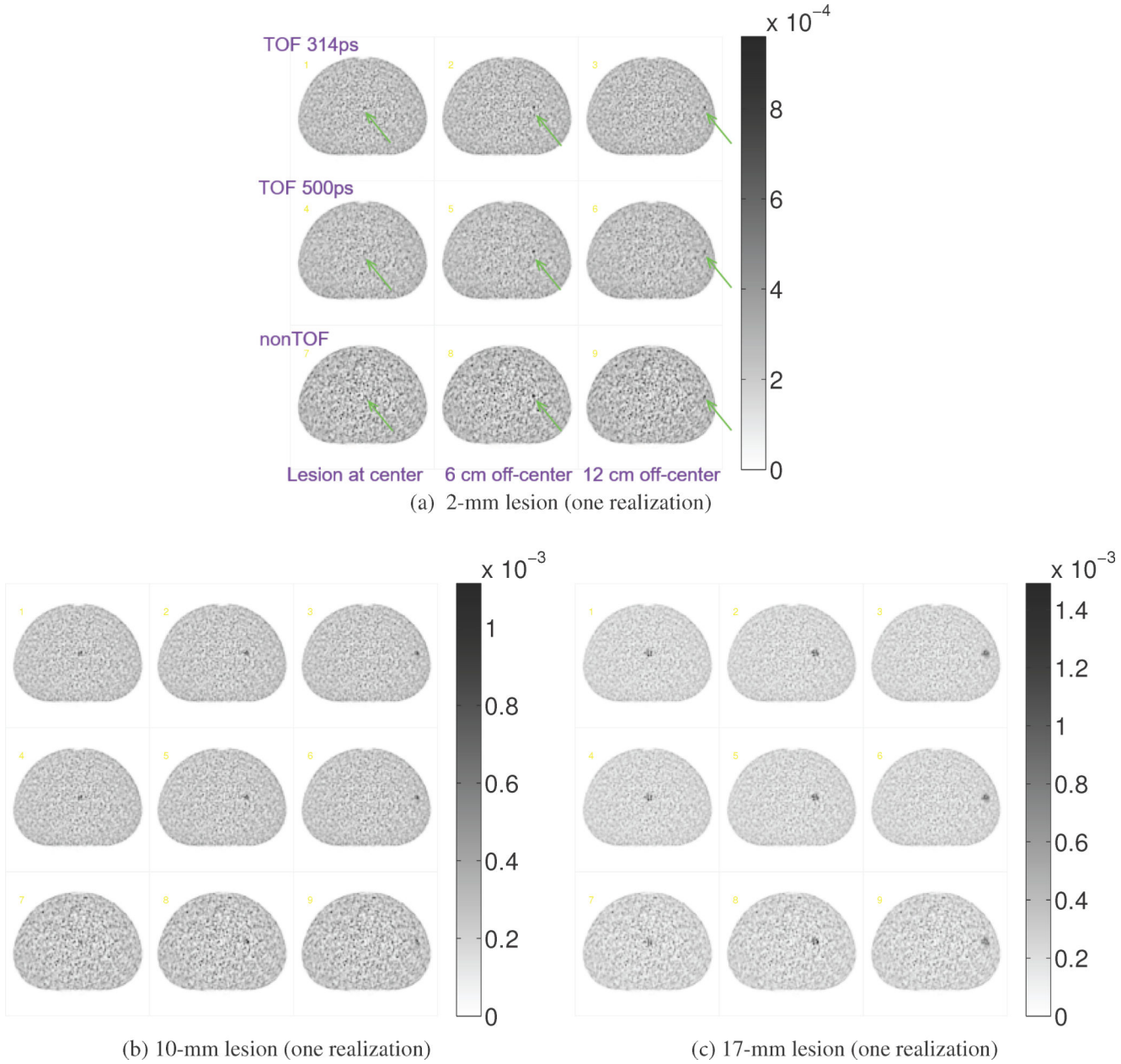

(a) 2-mm lesion (one realization)

(b) 10-mm lesion (one realization)

(c) 17-mm lesion (one realization)

Figure 4.

Reconstructed images of one realization of the NEMA body phantom with (a) 2-mm, (b) 10-mm and (c) 17-mm spherical hot inserts at three different radial positions (left: 0 mm, middle: 60 mm and right: 120 mm). Inside of each panel, top row: 314 ps TOF resolution; middle row: 500 ps TOF resolution; bottom row: non-TOF.

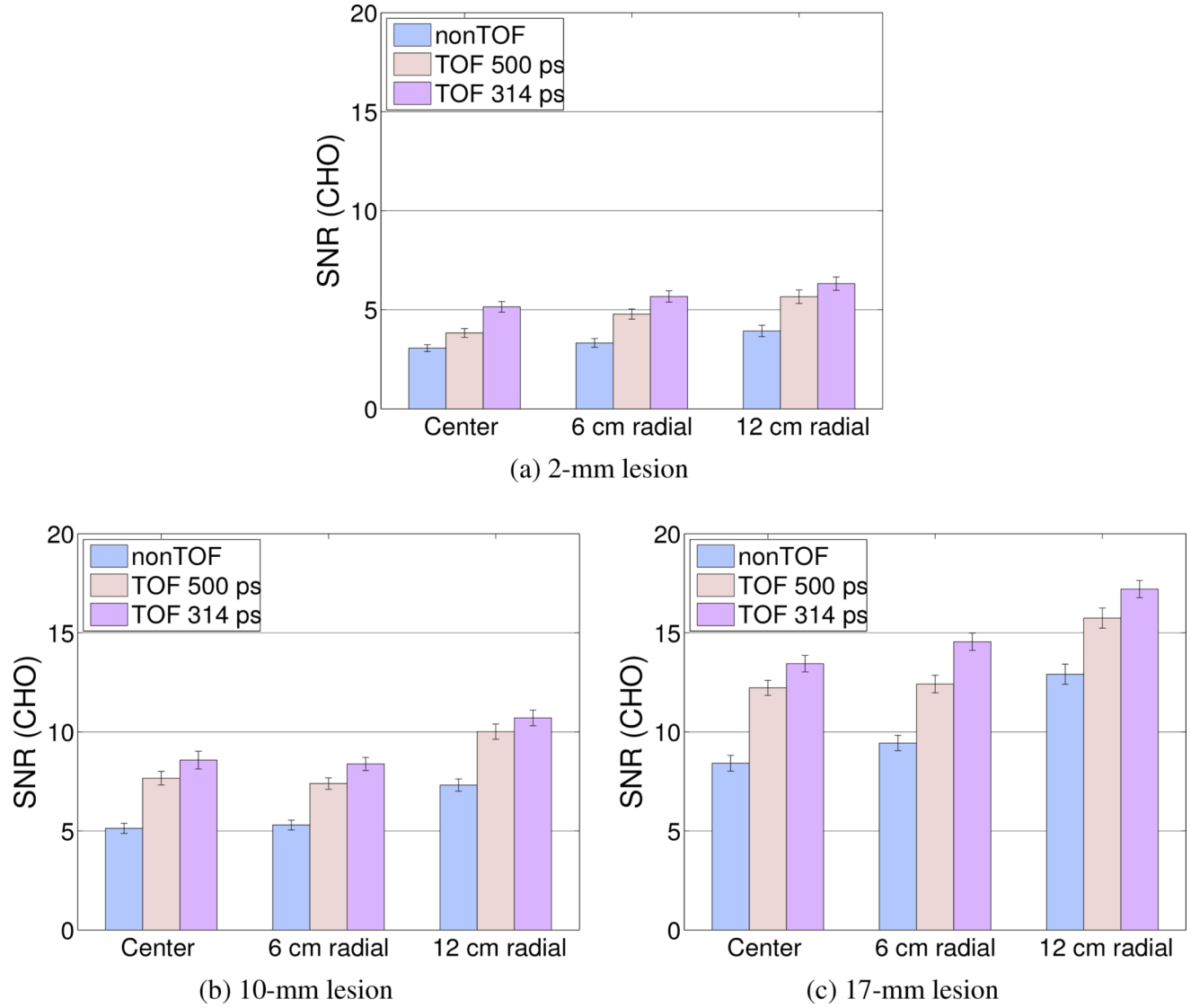

Figure 5.
CHO-SNR of lesion detection in the phantom study for (a) 2-mm lesion, (b) 10-mm lesion, and (c) 17-mm lesion.

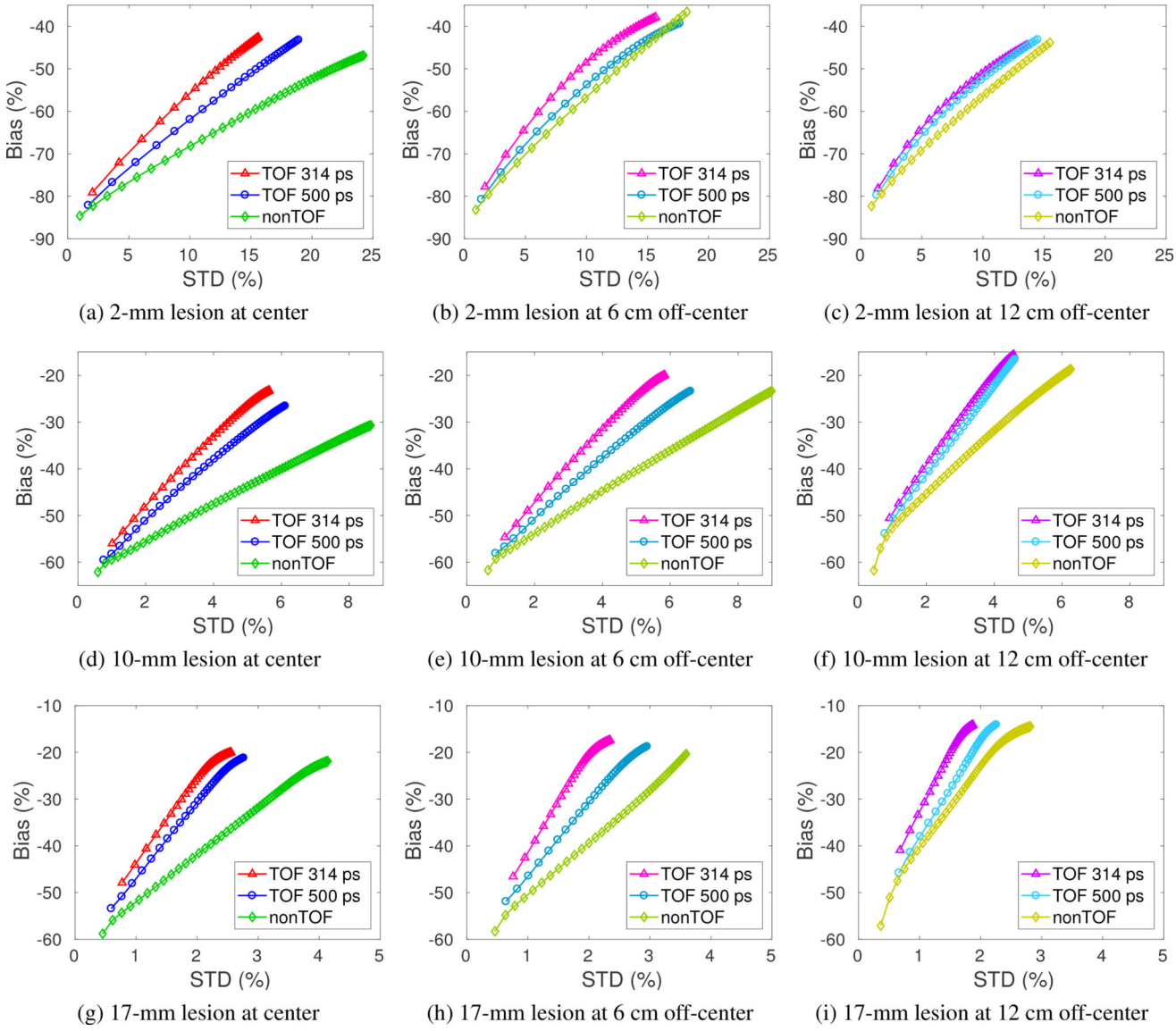

Figure 6.

The bias versus STD trade-off curves of the ROI quantification of TOF and non-TOF reconstruction in the phantom study for lesions of 2-mm (top row), 10-mm (middle row) and 17-mm (bottom row) at radial locations of center (left column), 6 cm off-center (middle column) and 12 cm off-center (right column). (Markers on the curves represent varied iterations of image reconstruction.)

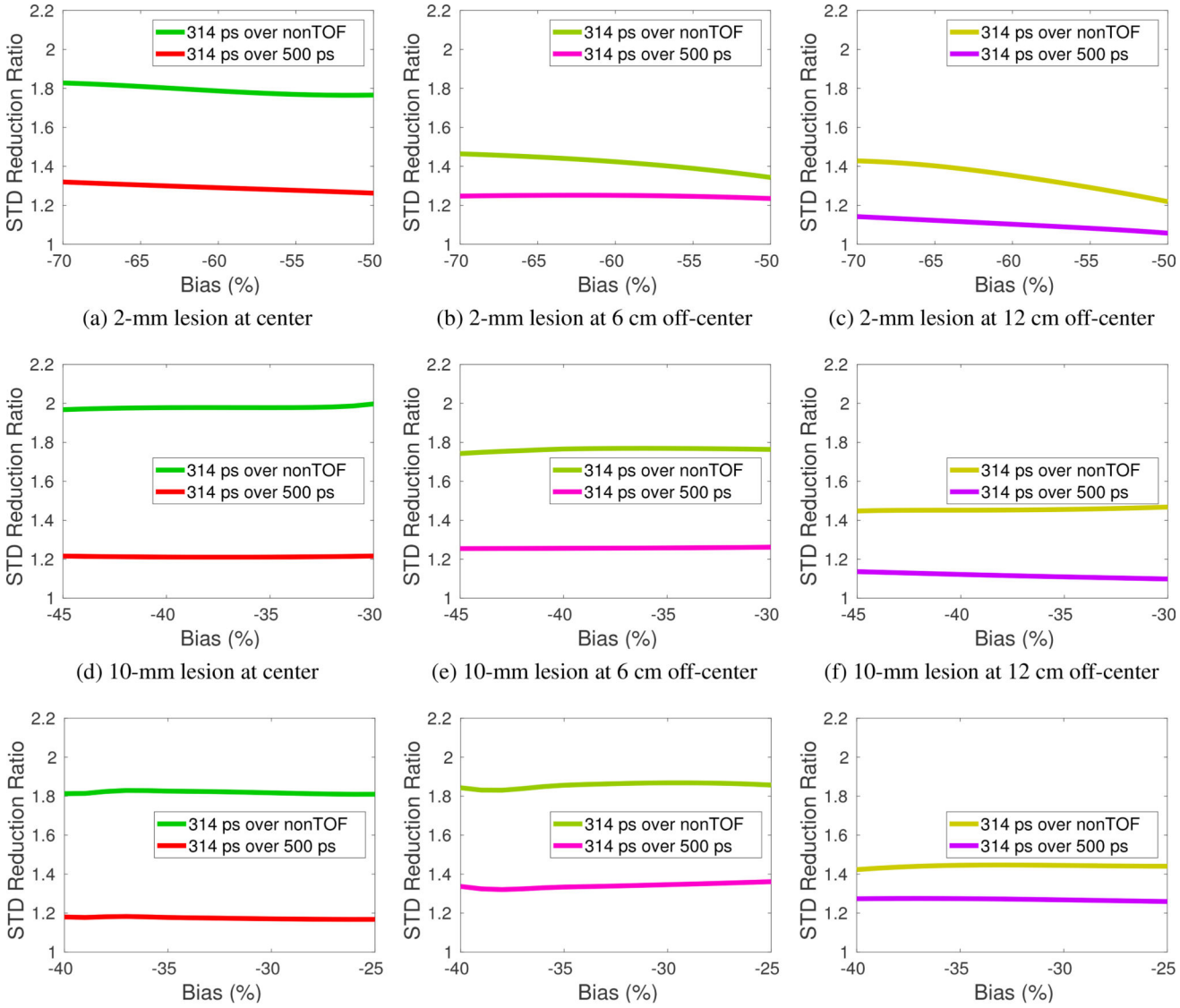

Figure 7.

STD reduction ratio over a range of bias for TOF 314 ps over 500 ps and non-TOF in the phantom study for the lesion sizes of 2-mm (top row), 10-mm (middle row) and 17-mm (bottom row) at radial locations of center (left column), 6 cm off-center (middle column) and 12 cm off-center (right column).

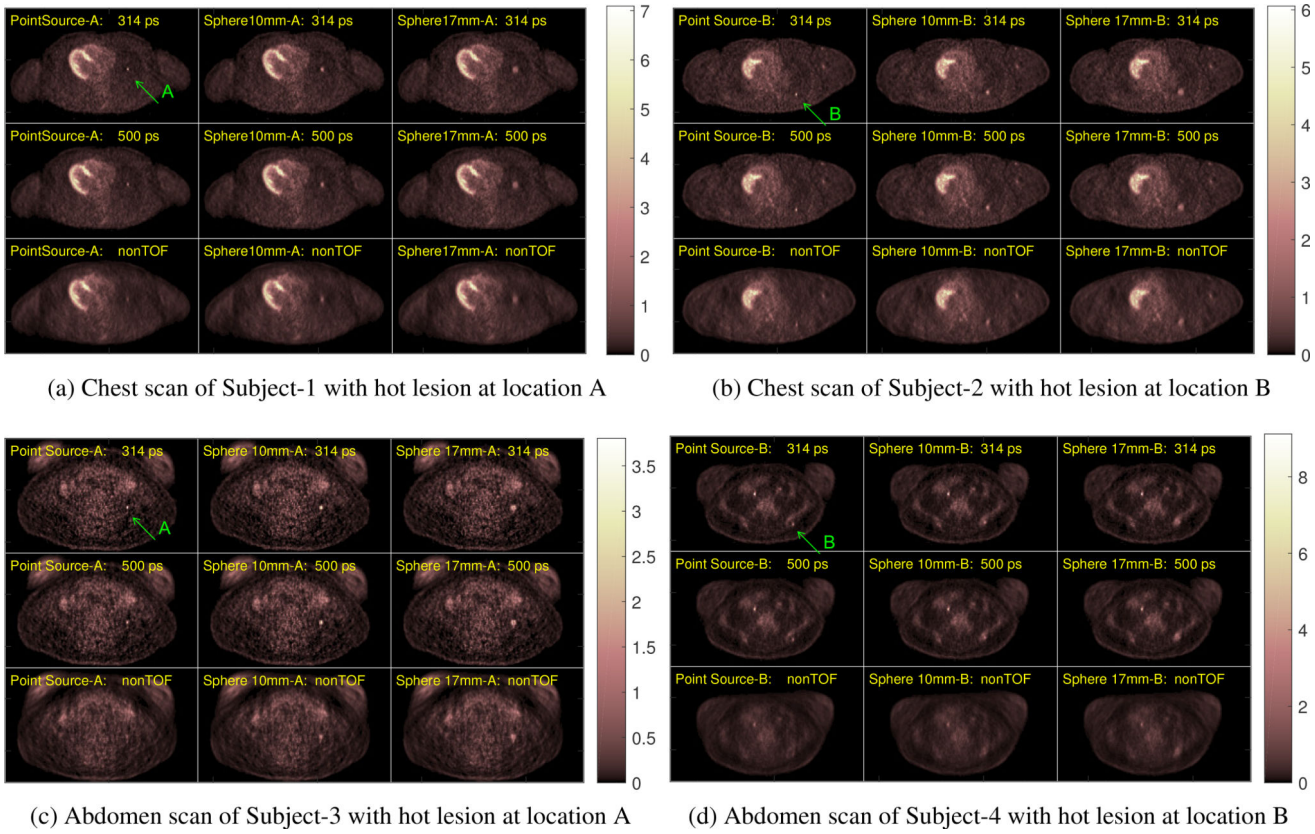

(a) Chest scan of Subject-1 with hot lesion at location A

(b) Chest scan of Subject-2 with hot lesion at location B

(c) Abdomen scan of Subject-3 with hot lesion at location A

(d) Abdomen scan of Subject-4 with hot lesion at location B

Figure 8.

Reconstructed images of the human study of chest scans (a,b) and abdomen scans (c, d) with a point source or hot sphere added. For each subject, from top to bottom, the images correspond to 314 ps TOF, 500 ps TOF, nonTOF, respectively; from left to right, the images contain a 1.0-mm point source, 10-mm sphere, 17-mm sphere, respectively.

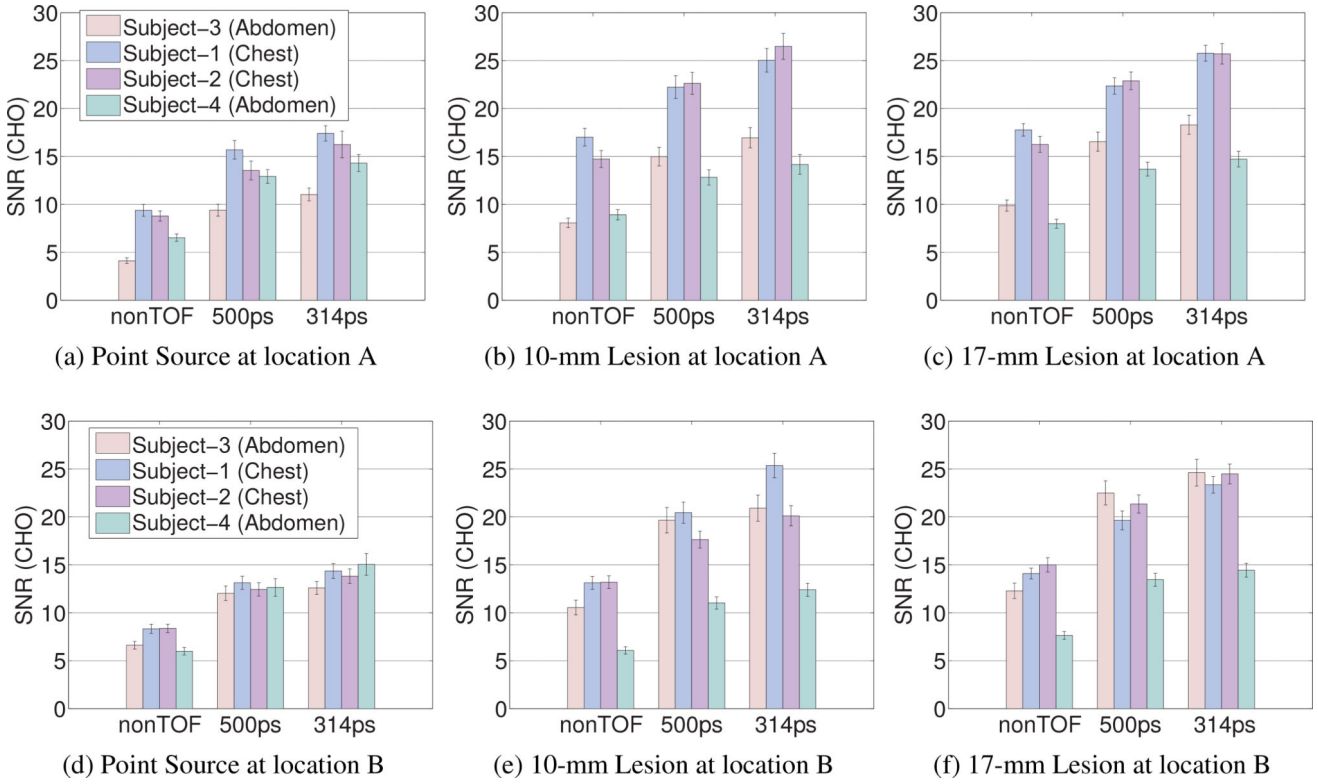

Figure 9.

Comparison of CHO-SNR between different TOF capability, lesion size and varied locations in four human subjects.

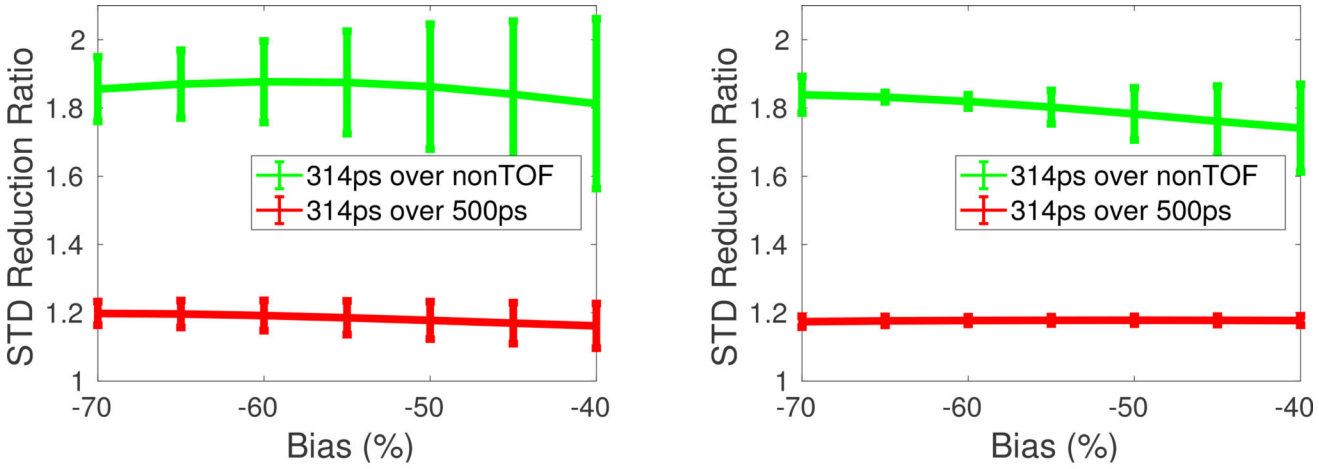

(a) 10-mm lesion (b) 17-mm lesion

Figure 10.

STD reduction factor on the ROI quantification in the human study for the 10-mm and 17-mm lesions averaged over two locations and four subjects.

Table 1

SNR gain ratio of 314ps over 500ps and non-TOF cases (2-mm and 10-mm lesions)

TOF Gain of CHO-SNR	Radial Location from Center		
	0 cm	6 cm	12 cm
314 ps over 500 ps (2mm lesion)	1.34±0.08	1.19±0.05	1.12±0.04
314 ps over nonTOF (2mm lesion)	1.68±0.11	1.71±0.14	1.61±0.14
314 ps over 500 ps (10mm lesion)	1.12±0.05	1.13±0.05	1.07±0.05
314 ps over nonTOF (10mm lesion)	1.67±0.12	1.58±0.08	1.46±0.09

Table 2

TOF gain of CHO-SNR on lesion detection of two locations of four human subjects

TOF Benefit	Lesion Size	CHO-SNR Gain Ratio
314ps over500ps	point	1.13±0.04
	10 mm	1.17±0.04
	17 mm	1.15±0.03
314ps over nonTOF	point	1.76±0.09
	10 mm	1.67±0.19
	17 mm	1.58±0.08